scientific reports

OPEN

Enhanced performance of flexible $BiFeO_3$ ferroelectric memory with Mica substrate via $SrTiO_3$ buffer layer

Xingpeng Liu[1], Yiming Peng[1], Fabi Zhang[1], Tangyou Sun[1], Ying Peng[1]✉, Lei Wen[2]✉ & Haiou Li[1]✉

$BiFeO_3$ (BFO) application in flexible wearable devices is garnering interest because of its unique ferroelectric and magnetic properties. However, the integration of high-quality BFO films onto flexible substrates presents significant technical challenges. Here, we successfully fabricated high-quality BFO films on mica substrates by using pulsed laser deposition, and report the fatigue characteristics of BFO films on flexible substrates for the first time. The results demonstrated that, after 10^8 bipolar switching cycles, the polarization only degraded by 0.28%, indicating superior fatigue characteristics compared to previously reported BFO films. Additionally, the device ferroelectric properties remained largely unchanged, with a bending radius of 3.5 mm. The fabricated flexible Pt/BFO/$La_{0.65}Sr_{0.35}MnO_3$(LSMO)/$SrTiO_3$(STO)/mica non-volatile memory devices exhibited mechanical flexibility and fatigue resistance. These findings not only highlight the potential of flexible BFO films for wearable electronic devices and flexible memory devices, they also provide valuable insight for the future development of high-performance flexible ferroelectric materials.

Keywords $BiFeO_3$ film, Flexible substrate, Pulsed laser deposition, Ferroelectric properties, Non-volatile memory

Ferroelectric random-access memory (FeRAM) is emerging as a popular next-generation memory technology owing to its rapid read/write speeds, high-density storage, and low power consumption. With the advent of the information age, the demand for memory has dramatically increased and conventional memory technologies have struggled to meet the current requirements of high speed, large capacity, and low power consumption. With its unique working principle and superior performance, FeRAM has immense potential and broad market prospects in the information storage sector[1–4]. As electronic technology continues to advance, the need for flexibility, miniaturization, and portability in next-generation electronic devices continues to increase, further exciting interest in flexible and wearable electronics[5–8]. Conventional rigid substrates face challenges, such as those related to size reduction and increased power consumption, whereas flexible substrates offer a new solution. Particularly, flexible electronic devices are entering a period of rapid development, with numerous materials being integrated onto flexible substrates. Such substrates exhibit excellent mechanical stability, allowing electronic devices to function in various deformation environments, such as bending and stretching, thereby enabling integration into bendable and wearable electronic products and providing flexibility in design and application. However, flexible substrates still face challenges regarding their high-temperature stability and compatibility with epitaxial films. High-quality functional oxide films typically require specific lattice orientations and high deposition temperatures to achieve crystalline growth[9–13]. To address these challenges, two approaches have been developed: wet etching of the sacrificial layers and film transfer[14–17]. In 2020, Ruonan et al. used deionized water to etch away a $Sr_3Al_2O_6$ sacrificial layer to obtain high-quality single-crystal $BaTiO_3$ films and Pt/$BaTiO_3$/PEDOT: PSS multilayer structures. Through their method, they achieved the heterogeneous integration of the film with a flexible substrate. The transferred $BaTiO_3$ film retained its single-crystal state and exhibited significant ferroelectric hysteresis under both flat and bent conditions[18]. The second is direct deposition on flexible substrates, however, direct deposition of oxide films on flexible substrates such as polyimide (PI) is challenging because PI substrates tend to bend at high temperatures, which is not conducive to film crystallization and growth. Mica is

[1]Guangxi Key Laboratory of Precision Navigation Technology and Application, Guilin University of Electronic Technology, Guilin 541004, China. [2]The 10th Research Institute of CETC, Chengdu 610036, China. ✉email: pengying@guet.edu.cn; wenlei2324@163.com; lihaiou@guet.edu.cn

a silicate mineral with a layered structure that offers several advantages as a flexible substrate. Mica has a high melting point (approximately 1200–1300 °C), good stability and mechanical strength at high temperatures, and excellent insulating properties[19]. Its layered structure provides good flexibility, giving it potential for applications in wearable electronics. Although conventional hafnium-based ferroelectric films possess excellent ferroelectric properties, their strong wake-up effect and fatigue effect limit their applicability[20,21]. Perovskite ferroelectric films, such as $BaTiO_3$ films, are known for their outstanding ferroelectric performance and reliability. $BaTiO_3$ is stable at high temperatures, exhibits excellent fatigue resistance, and has been successfully grown epitaxially on both rigid and flexible substrates[22]. However, its low spontaneous polarization value (~ 20 μC/cm^2) limits its applicability[23]. Although Pb(Zr, Ti)O_3 offers high polarization, a low coercive field, and fatigue resistance, it is not environmentally friendly owing to its lead content, and it poses contamination risks during fabrication[24–28]. $BiFeO_3$ (BFO) has gained prominence among ferroelectric materials owing to its high spontaneous polarization (~ 100 μC/cm^2) and lead-free composition[29–31]. Additionally, BFO films prepared on rigid substrates exhibit poor fatigue resistance. Addressing these challenges requires suitable bottom electrodes and buffer layer[35]. Flexible BFO ferroelectric memories have demonstrated significant application potential and research value. Their development addresses the key challenges in flexible electronic technology and offers a promising solution for future electronic device applications.

We have developed a flexible mica substrate-based BFO ferroelectric memory device by successfully fabricating a high-quality (111) BFO / (111) $La_{0.65}Sr_{0.35}MnO_3$ (LSMO) / (111) $SrTiO_3$ (STO)heterostructure. We conducted a comprehensive study on the ferroelectric properties and fatigue characteristics of the device under flat conditions and various bending radii. The results indicate that the ferroelectric properties and fatigue resistance of the device remained essentially unchanged when bent. After 10^8 bipolar switching cycles, the device showed no signs of fatigue and exhibited the best fatigue resistance among the reported BFO materials[36,37]. Moreover, the electric hysteresis loops of the device exhibited negligible changes under different bending radii, indicating that the fabricated device maintained its performance under bending or other complex conditions. Thus, this device has significant potential for application in flexible and wearable electronic devices.

Materials and methods

Device preparation process

The mica substrate was sequentially ultrasonically cleaned with acetone, absolute ethanol, and deionized water, 10 min for each cleaning process. After cleaning, the mica substrate was dried with a nitrogen gun and then placed into a pulsed laser deposition (PLD) growth chamber for the deposition of STO and LSMO. After the deposition, a portion of the LSMO was masked to serve as the bottom electrode. The substrate was then returned to the chamber to continue the growth of BFO. Lastly, radio-frequency magnetron sputtering was used to deposit a 70 μm × 70 μm Pt top electrode on the surface of the BFO film.

Film deposition parameters

The STO, LSMO, and BFO films were deposited on mica substrates by operating a PLD system (PLD-S40-L, Beijing Perfect Technology Co., Ltd.) with a KrF excimer laser at a wavelength of 248 nm. The buffer layer STO was first deposited on the substrate at 750 °C under an oxygen pressure of 10 Pa. Subsequently, LSMO was epitaxially grown on the STO film at 750 °C. The ferroelectric layer BFO was then epitaxially grown on the LSMO film at 650 °C. The heterojunction was annealed in situ at 600 °C under an oxygen pressure of 60 Pa for 30 min, followed by cooling to room temperature at a rate of 7 ℃/min.

Test equipment

The phase structure of the BFO/LSMO/STO/mica heterojunction was analyzed by applying X-ray diffraction (XRD, Bruker D8Advance, Germany) with Cu Kα radiation ($\lambda = 1.5405$ Å). The voltage and current were set at 40 kV and 40 mA, respectively, with a scanning step size of 0.01°. The optical transmittance of the device was measured at different wavelengths by applying UV-Vis spectrophotometry (Perkin Elmer Lambda 365). The surface morphology and roughness of the films were analyzed by using atomic force microscopy (AFM; Cypher S/Oxford Instruments Asylum Research); the ferroelectric domain switching and phase and amplitude measurements of the BFO films were performed under the SSPFM mode. Optical microscopy (Nikon Eclipse LV150N) was used to examine the integrity of the electrode patterns following ultraviolet lithography, and scanning electron microscopy (Zeiss Sigma 300/Nergy Oxford 30 Xplore) yielded high-resolution images of the device surface at an acceleration voltage of approximately 3 kV. Additionally, the elemental distribution and crystal structure within the device were determined by using transmission electron microscopy (TEM, FEI Tecnai G2 F20) and energy-dispersive X-ray spectroscopy (EDS, Bruker XFlash 5030), respectively. The current–voltage (I–V) characteristics of the device were measured by using a Keithley 2400 digital source meter to evaluate its electrical performance. The ferroelectric properties, which are key indicators of BFO films, were precisely quantified by using a HUACE FE-2000 ferroelectric analyzer.

Results and discussion

Figure 1a shows the structural diagram of the BFO/LSMO/STO/mica heterojunction. The crystal orientation of the BFO/LSMO/STO/mica multilayer structure was determined by using XRD. Figure 1b presents a typical out-of-plane θ–2θ linear scan of the multilayer film. In addition to the (00 L) peaks from the mica substrate, only the diffraction peaks of (111) BFO/ (111) LSMO/ (111) STO were observed, with no other extraneous peaks, indicating that the prepared films had single-crystal structures. Moreover, based on the XRD results, we calculated the interplanar spacings of the various layers in the heterostructure; particularly, BFO (d (111) = 2.300 Å) had a mismatch rate of approximately 0.37% relative to the standard card, LSMO (d (111) = 2.250 Å) had a

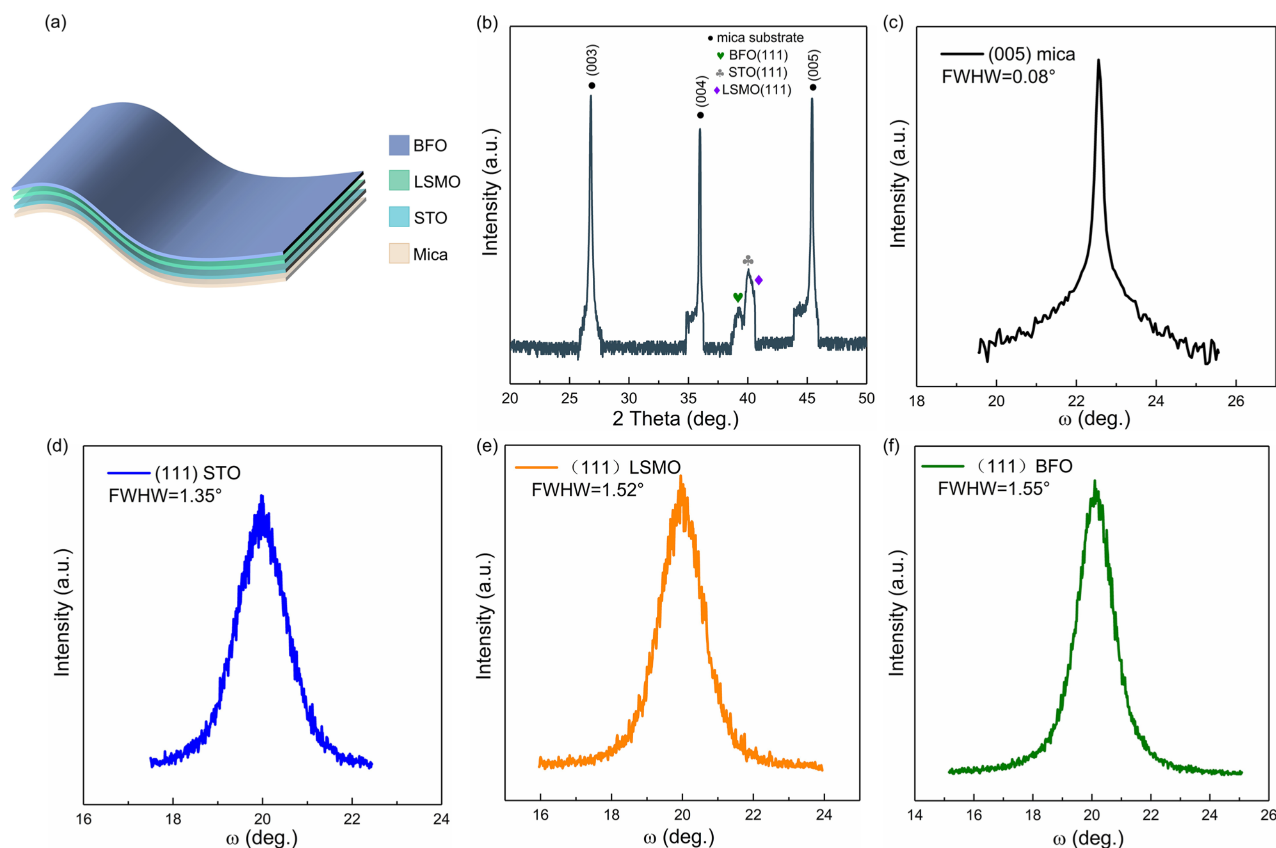

Fig. 1. (**a**) Schematic diagram of BFO/LSMO/STO/mica heterostructure. (**b**) XRD pattern of BFO/LSMO/STO/mica heterostructure. XRD ω-scan of (**c**) mica substrate, (**d**) STO thin film, (**e**) LSMO thin film, (**f**) BFO thin film.

mismatch rate of approximately 0.45%, and STO (d (111) = 2.255 Å) had a mismatch rate of only 0.05%. These calculations indicate that our films achieved good epitaxial growth on the mica substrate, and that the slight differences in the actual interplanar spacing relative to the standard card values were attributable to in-plane tensile strain[39–41]. Figure S1 shows the XRD patterns of the BFO/LSMO/mica heterostructure, where only the diffraction peaks of the mica substrate are observed. This indicates that the BFO and LSMO films failed to crystallize, likely due to the significant lattice mismatch between LSMO and mica. By inserting an STO buffer layer, we successfully fabricated (111)-oriented BFO films. This method establishes a foundation for the good ferroelectric performance of flexible BFO devices. Supplementary Figure S2 complements the XRD plots of the BFO film at 600 ℃ versus 680 ℃ and the ω-scan test plot of the BFO film at 600 ℃. XRD φ scan patterns for STO (200) peak was showed in Supplementary Figure S3.

Supplementary Figure S4 complements the AFM plots of BFO films at 600 ℃, 650 ℃ and 680 ℃, showing that the BFO films prepared at 650 ℃ have the least roughness. The ω-scan was used to characterize the film's full width at half maximum (FWHM). Figure 1c shows that the FWHM of the (005) mica substrate is only 0.08°, which provides a foundation for the quality of the subsequent epitaxial films. The FWHM results of epitaxial films was showed in Fig. 1d,e, indicating that the prepared films exhibited good in-plane and out-of-plane orientation consistency, demonstrating high crystallinity. Supplementary Figure S5 complements the SEM image of the film surface of the BFO film at 650 ℃.

To further elucidate the epitaxial growth behavior of the BFO/LSMO/STO/mica heterojunction, we conducted high-resolution cross-sectional TEM (i.e., HRTEM) analysis. Figure 2a shows a cross-sectional image of the heterojunction in which the layers are tightly bonded with distinct interfaces. From bottom to top, the sequence of layers was as follows: mica substrate, STO, LSMO, and BFO. The clear interface between the STO buffer layer and mica substrate provides a robust foundation for the single-crystal epitaxy of BFO and LSMO on mica. To determine the elemental distribution within each film layer, we applied EDS to Bi, Mn, and Ti. Figure 2b–d present the EDS scan results, showing distinct elemental boundaries without significant diffusion, with the elements concentrated in their respective regions. Supplementary Figure. S6 shows the EDS scans for Fe, La, and Sr.

As shown in Fig. 2e–g, the HRTEM analysis of the BFO/LSMO/STO/mica heterostructure revealed clear and distinct interfaces between the different layers. A magnified view of the interface between the mica and STO (Fig. 2e) revealed a clear lattice structure, and the result of applying a fast Fourier transform (FFT) to the electron diffraction pattern confirmed the single-crystal nature of STO, revealing (001), (111), and (110) planes.

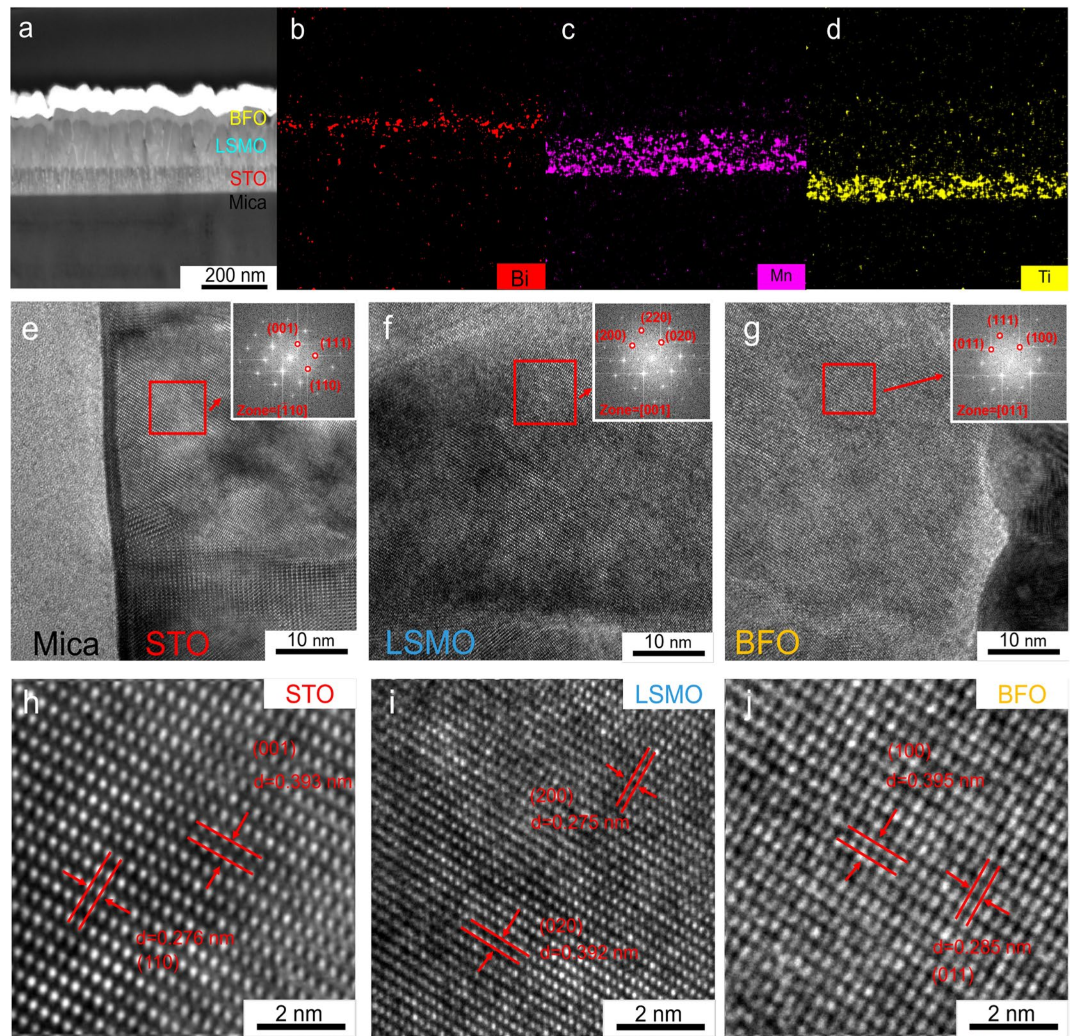

Fig. 2. (**a**) Cross-sectional TEM image of BFO/LSMO/STO/mica heterostructure. (**b**–**d**) EDS mappings of Bi, Mn, and Ti, respectively, in BFO/LSMO/STO/mica heterostructure. (**e**) HRTEM image and FFT pattern of mica/STO interface. (**f**) HRTEM image and FFT pattern of STO/LSMO interface. (**g**) HRTEM image and FFT pattern of LSMO/BFO interface. (**h**–**j**) Atomic-scale HRTEM image of STO, LSMO, and BFO layers.

Figure 2f presents an HRTEM image of the LSMO layer, where a clear lattice structure is visible in the magnified view and the corresponding electron diffraction pattern revealed (200), (220), and (020) planes. Figure 2g shows the BFO layer, highlighting a clear lattice structure, and with the corresponding electron diffraction pattern revealing (011), (111), and (001) planes. Figure 2h–j provide detailed HRTEM images of the STO, LSMO, and BFO layers, respectively, with marked interplanar spacings; particularly, in STO, the (110) and (001) planes had lattice spacings of 0.276 nm and 0.393 nm, respectively; in LSMO, the (020) and (200) planes had lattice spacings of 0.392 nm and 0.275 nm, respectively; in BFO, the (011) and (100) planes had lattice spacings of 0.285 nm and 0.395 nm, respectively. These detailed HRTEM images and the corresponding diffraction patterns are crucial for understanding the high-quality crystallinity of each layer in the BFO/LSMO/STO/mica heterostructure. HRTEM analysis of the BFO/LSMO/STO/mica heterostructure not only demonstrates the high-quality crystallinity and sharp interfaces of each layer, it also facilitated further understanding of the principles of growth and integration of complex oxide materials. This information is essential for advancing the development of next-generation multifunctional devices. Supplementary Figure S7 illustrates a test plot of the optical transmittance of the BFO/LSMO/STO/mica heterostructure.

BFO ferroelectric films, with their high spontaneous polarization at room temperature and good structural stability, have significant potential for application in electronic devices and non-volatile memories. However, a significant challenge at room temperature is the high leakage current of BFO films. This high leakage current can strongly suppress the ferroelectric polarization effect and degrade the related electrical performance. The key to overcoming this problem is the fabrication of high-quality single-crystal BFO films[42–46]. Figure 3a shows the *I*–*V* characteristics of the BFO/LSMO/STO/mica heterojunction. The fabricated devices exhibited low leakage currents, indicating that we successfully fabricated high-quality single-crystal BFO films by designing the appropriate buffer layers. The *I*–*V* curve for the device indicated pronounced hysteresis, which has been attributed

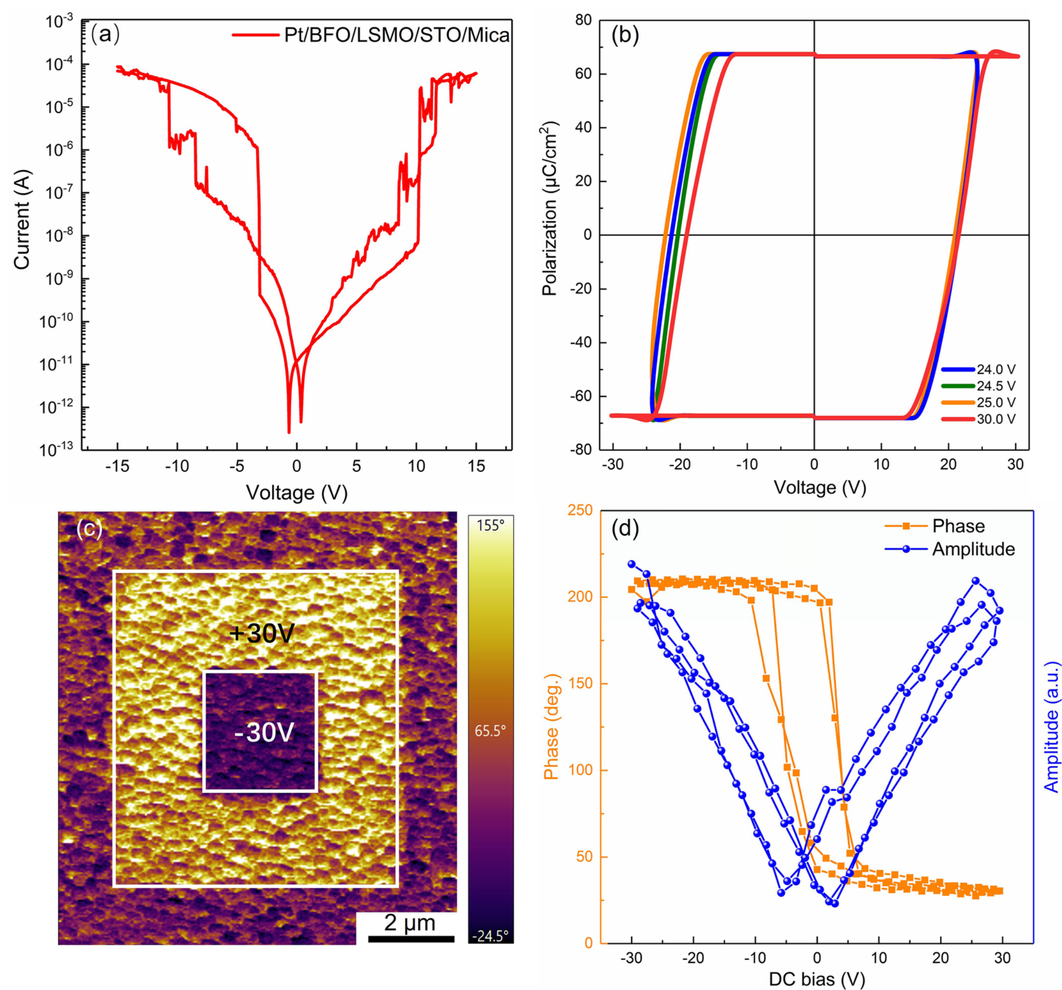

Fig. 3. (**a**) *I*–*V* characteristics of BFO/LSMO/STO/mica heterojunction. (**b**) *P*–*V* hysteresis loops for flexible BFO thin-film memory. (**c**) PFM phase image of BFO thin film. (**d**) Phase–amplitude curve for BFO film.

to changes in resistance induced by the ferroelectric polarization characteristics. Under a strong electric field, the direction of the ferroelectric domains fully reversed, altering the polarization state and significantly increasing the current. The asymmetry in the *I*–*V* curve may be attributable to the different barrier heights at the electrode/BFO interface under varying polarization states. This asymmetry is also commonly observed in ferroelectric resistive switching behavior, which is consistent with previous reports[47].

Figure 3(b) shows the polarization versus voltage (*P*–*V*) loops for the flexible BFO thin-film memory device at different voltages and a frequency of 1 kHz. The curves exhibited distinct rectangular hysteresis loops, indicating the significant ferroelectric properties of BFO. As the electric field changed from negative to positive, the polarization reversed, manifesting as symmetric loops in the *P*–*V* curves. Higher applied voltages contributed to circumvent the effects of the coercive field, leading to rapid polarization switching. By increasing the voltage, we observed the *P*–*V* curves to tend toward saturation polarization switching also became more pronounced. At 25 V, the flexible Pt/BFO/LSMO/STO/mica device exhibited a remnant polarization ($2P_r$) of 134 $\mu C/cm^2$ and saturated polarization ($2P_{max}$) of approximately 138 $\mu C/cm^2$. Notably, these polarization values were higher than those for many previously reported (111) and (100) orientations BFO films grown on rigid substrates[32–37]. The polarization value of BFO films is closely related to their growth orientation, and the maximum theoretical polarization value of BFO films along the (111) orientation can reach 100 ($\mu C/cm^2$)[38].

Comprehensive characterization and analysis of heterostructures provide significant guidance for the subsequent fabrication of flexible smart wearable devices. Figure 3(c) shows the PFM image of the ferroelectric BFO film. The two different colors represent the different switched states of the ferroelectric domains with a 180° phase difference between them, confirming the switchable polarization and good nanoscale ferroelectricity of the BFO ferroelectric film[48,49].

The amplitude–phase curve for the BFO film was showed in Fig. 3d. The amplitude curve exhibited a butterfly-shaped pattern, indicating bidirectional changes in polarization under the influence of the electric field. This result is consistent with those of previous studies, further confirming the ferroelectricity of BFO ferroelectric film[50,51].

The *P*–*V* hysteresis loops and transient currents for BFO are shown in Fig. 4a. Near the coercive fields (V_c) of ± 15 V, distinct diametrically opposed transient current peaks can be observed. When the applied voltage reached the coercive field value, significant reorientation of the electric dipoles within the material occurred, leading to transient current spikes. This phenomenon occurred because the dipoles switched directions, causing a temporary increase in the current. The formation of these transient current peaks further confirms the ferroelectric properties of the flexible BFO memory devices[42].

The retention characteristics directly affect the reliability of the ferroelectric memory data. Ferroelectric memory stores information in the polarization direction, and good retention characteristics indicate that the stored information can be preserved without loss or degradation over time. To comprehensively evaluate the reliability of the flexible Pt/BFO/LSMO/STO/mica device, we analyzed the retention characteristic curve under a bias voltage of 2 V and pulse width time of 100 ms (Fig. 4b). The results indicate that the flexible BFO ferroelectric memory demonstrates good stability and reliability over time. Across a long range of retention times, the polarization value remained consistent, highlighting the potential of this material for non-volatile memory applications for which data integrity and long-term storage are critical. These characteristics ensure that BFO memory devices satisfy the demands of various high-performance and high-reliability electronic applications.

We conducted electrical tests on the device in both flat and bent states to evaluate its performance under bending conditions. Supplementary Figure S8 shows a physical diagram of a flexible device wearable. Supplementary Figure S9 shows the bending tests results for the flexible Pt/BFO/LSMO/STO/mica device on molds with bending radii of 6 mm and 3.5 mm, respectively. The *P*–*V* hysteresis loops for the flexible BFO device at a test frequency of 1 kHz and voltage of 20 V in the flat and various bending radii states are shown in Fig. 5a. The properties of ferroelectric materials are generally strongly dependent on their lattice structures. Stress can cause lattice distortion and alter the atomic positions and lattice constants, thereby affecting the arrangement and switching process of electric dipoles. Because ferroelectric polarization is induced by the directional alignment of electric dipoles, lattice distortion directly affects the polarization strength and shape of the hysteresis loop[52,53]. When bent to a radius of 3.5 mm, the hysteresis loop for the device broadened, indicating that the stress impacted the device, slightly weakening the polarization. At a bending radius of 6 mm, the hysteresis loop remained largely consistent with that in the flat state, with only minor changes. The results demonstrate that the fabricated flexible Pt/BFO/LSMO/STO/mica device exhibits good flexibility and mechanical robustness, maintaining its ferroelectric properties under various bending stresses, thus making it highly promising for flexible electronic applications.

In practical application, ferroelectric materials are often subject to repeated electric field applications, leading to the gradual degradation of their ferroelectric properties, known as the fatigue effect. Fatigue testing simulates this long-term usage, facilitating evaluation of the reliability and durability of the material under high-frequency switching operations. Understanding the fatigue behavior of materials ensures that the device will demonstrate stability throughout its lifespan. To assess the reliability of the fabricated flexible ferroelectric non-volatile memory device, we applied fatigue tests under 100 kHz square-wave conditions to devices in various bending states. Figure 5(b) illustrates the results for the unbent state; after 10^8 bipolar switching cycles, the device's 2*P*r value decreased from 135.33 to 135.09 μC/cm^2, a reduction of only 0.28%. Additionally, the 2*P*max value decreased from 138.36 to 135.19 μC/cm^2, a reduction of 2.30%. These results indicate good fatigue resistance.

Figure 5c,d show the fatigue test results for the device under different bending radii. These results were consistent with those for the unbent state (Fig. 5b). At a bending radius of 3.5 mm, after 10^8 cycles, the 2*P*r value decreased from 135.99 to 135.07 μC/cm^2, and the 2*P*max value decreased from 137.12 to 135.88 μC/cm^2. When

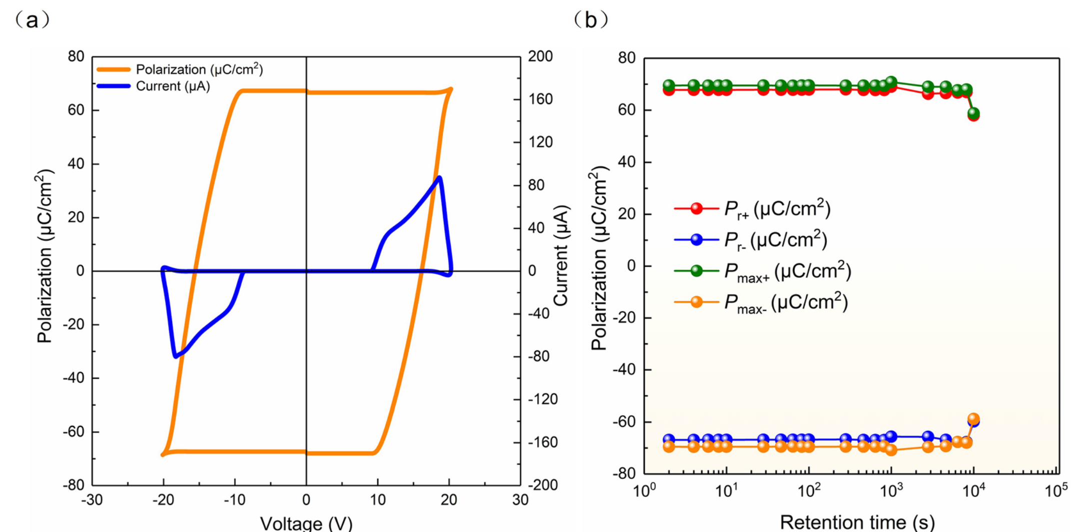

Fig. 4. (**a**) *P*–*V* hysteresis loop and transient current of BFO thin film. (**b**) Retention characteristic curves for flexible Pt/BFO/LSMO/STO/mica ferroelectric memories.

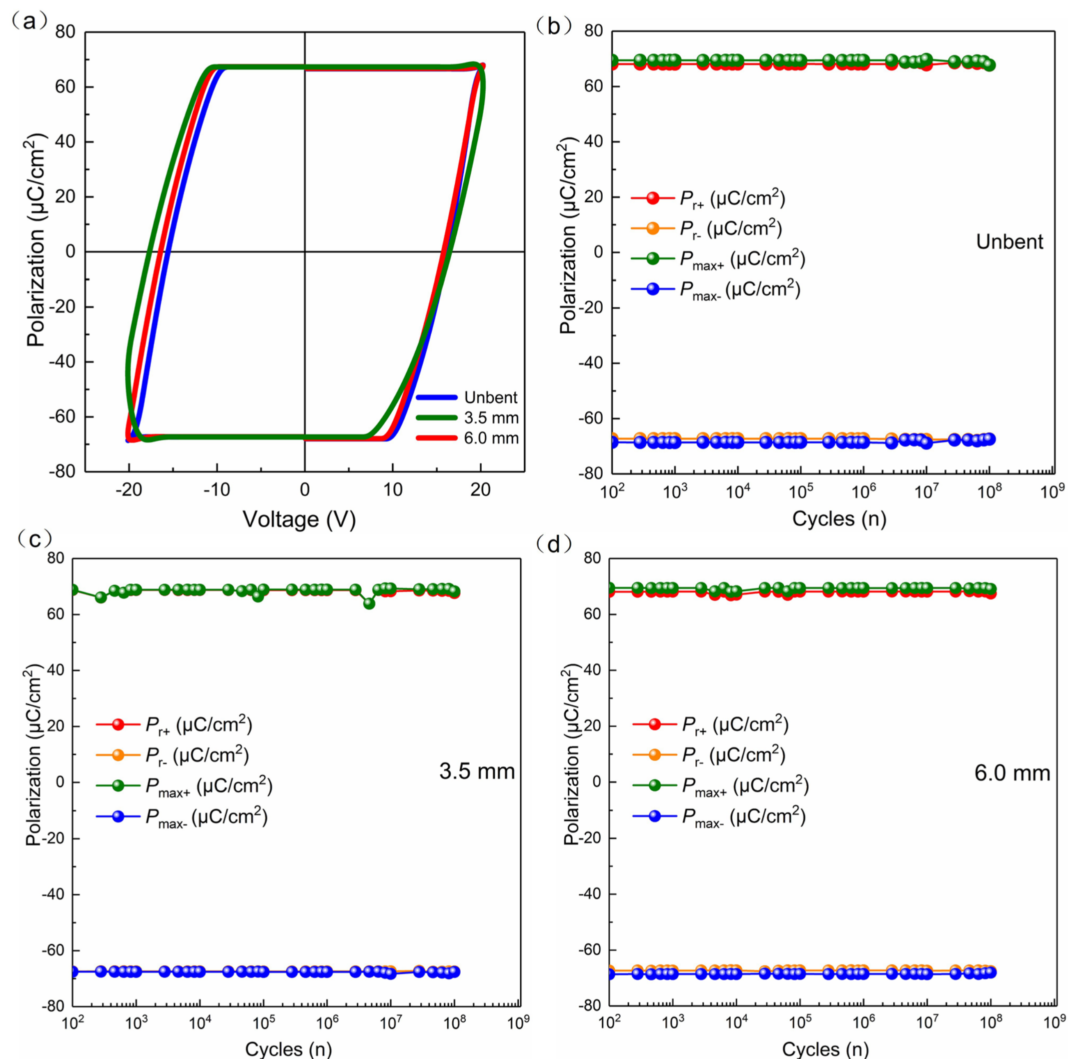

Fig. 5. (**a**) *P–V* hysteresis loops for flexible BFO memory under different bending conditions. (**b**) Fatigue characteristics of flexible BFO memory device in unbent state at 100 kHz. (**c**) Fatigue characteristics of flexible BFO memory device with 3.5 mm bending radius at 100 kHz. (**d**) Fatigue characteristics of flexible BFO memory device with 6.0 mm bending radius at 100 kHz.

the bending radius was adjusted to 6 mm, after 10^8 bipolar switching cycles, the changes in polarization values were minimal, with the 2*Pr* value decreasing from 135.48 to 135.01 μC/cm^2 and the 2*P*max value decreasing from 138.15 to 137.13 μC/cm^2. The comparison of the *P-V* loops of flexible BFO devices after release from the bent state and in the unbent state was presented in Figure S10. Figure 6a shows that the polarization value and coercive field (V_c) of the device remain essentially unchanged for different bending radii. Thus, the device exhibits good fatigue resistance, stability, and reliability under various bending conditions. This is the first report of the fatigue characteristics of BFO films on flexible substrates. Compared with other reported ferroelectric memory devices, as shown in Fig. 6b, our flexible BFO ferroelectric memory device demonstrates superior fatigue resistance and larger polarization values. Even under bending stress, the polarization characteristics remained largely unaffected and retained their memory retention capabilities. The fabricated device has a wide range of application prospects in non-volatile memory and wearable flexible electronics technologies.

Conclusions

We successfully obtained high-quality (111)-oriented BFO films on mica substrates by applying PLD with a rationally designed buffer layer. our fabricated Pt/BFO/LSMO/STO/mica device exhibited good performance, with 2*Pr* reaching 134 μC/cm^2 and 2*P*max reaching approximately 138 μC/cm^2. Previous studies have shown that the polarization capability of BFO ferroelectric films on rigid substrates begins to degrade after 10^6 cycles; however, our BFO films, which we directly fabricated on flexible substrates, maintained their polarization capability beyond 10^8 cycles, demonstrating exceptional fatigue resistance. During bending tests, the device performance did not significantly degrade; furthermore, the ferroelectric memory operated safely at a bending radius of 3.5 mm. In summary, owing to its high polarization, non-volatility, fatigue resistance, and flexibility,

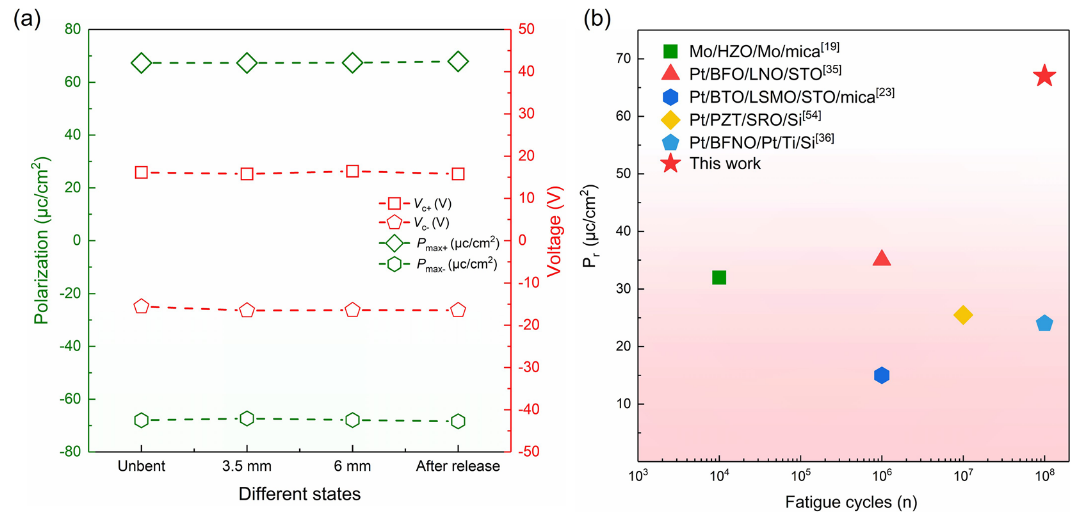

Fig. 6. (**a**) Comparison of the coercive field (V_c) and P_{max} values for BFO/LSMO/STO/mica devices at different bending radii. (**b**) Comparison of ferroelectric memory devices.

our flexible BFO ferroelectric memory device has significant prospects for application in flexible electronics and smart wearable devices.

Data availability
Data is provided within the manuscript or supplementary information files.

Received: 20 July 2024; Accepted: 21 October 2024
Published online: 25 October 2024

References
1. Jiang, J., Chai, X., Wang, C. & Jiang, A. High temperature ferroelectric domain wall memory. *J. Alloys Compd.* **856**, 158155. https://doi.org/10.1016/j.jallcom.2020.158155 (2021).
2. Li, Z. & Haas, Z. J. On residual path lifetime in Mobile Networks. *IEEE Commun. Lett.* **20**, 582–585. https://doi.org/10.1109/lcomm.2016.2520467 (2016).
3. Park, J. Y. et al. Revival of ferroelectric Memories based on emerging Fluorite-structured ferroelectrics. *Adv. Mater.* **35**, e2204904. https://doi.org/10.1002/adma.202204904 (2023).
4. Sharma, P. et al. Nonvolatile ferroelectric domain wall memory. *Sci. Adv.* **3** https://doi.org/10.1126/sciadv.1700512 (2017).
5. de Marzo, G. et al. Sustainable electronic biomaterials for body-compliant devices: challenges and perspectives for wearable bio-mechanical sensors and body energy harvesters. *Nano Energy*. **123**, 109336. https://doi.org/10.1016/j.nanoen.2024.109336 (2024).
6. Hu, J. & Dong, M. Recent advances in two-dimensional nanomaterials for sustainable wearable electronic devices. *J. Nanobiotechnol.* **22**. https://doi.org/10.1186/s12951-023-02274-7 (2024).
7. Xiao, W. et al. Thermally stable and Radiation Hard Ferroelectric $Hf_{0.5}Zr_{0.5}O_2$ Thin films on Muscovite Mica for flexible nonvolatile memory applications. *ACS Appl. Electron. Mater.* **1**, 919–927. https://doi.org/10.1021/acsaelm.9b00107 (2019).
8. Yun, J. Recent progress in thermal management for flexible/wearable devices. *Soft Sci.* **3**. https://doi.org/10.20517/ss.2023.04 (2023).
9. Bakaul, S. R. et al. High speed Epitaxial Perovskite memory on flexible substrates. *Adv. Mater.* **29**. https://doi.org/10.1002/adma.201605699 (2017).
10. Jiang, Y. et al. Enabling ultra-low-voltage switching in $BaTiO_3$. *Nat Mater*. 21, 779–785. https://doi.org/10.1038/s41563-022-01266-6 (2022).
11. Sengupta, S., Ghatak, A. & Raychaudhuri, A. K. Effect of low temperature structural phase transitions in $BaTiO_3$ on electrical transport through a metal-ferroelectric-metal multilayer of AuCr/$BaTiO_3$/Nb:$SrTiO_3$. *J. Phys. Condens. Matter*. **33**. https://doi.org/10.1088/1361-648X/ac1d6e (2021).
12. Wang, X. et al. Effect of a semiconductor electrode on the tunneling electroresistance in ferroelectric tunneling junction. *Appl. Phys. Lett.* **109**, 163501. https://doi.org/10.1063/1.4965708 (2016).
13. Zhu, H., Kang, L., Liu, M. & Ouyang, J. Single-crystal oxide substrate dependent electrical properties of sputtered $BiFeO_3$ thin films. *Mater. Lett.* **174**, 57–60. https://doi.org/10.1016/j.matlet.2016.03.088 (2016).
14. Chiabrera, F. M. et al. Freestanding Perovskite Oxide films: synthesis, challenges, and Properties. *Ann. Phys.* **534**, 2200084. https://doi.org/10.1002/andp.202200084 (2022).
15. Gao, W., Zhu, Y., Wang, Y., Yuan, G. & Liu, J. M. A review of flexible perovskite oxide ferroelectric films and their application. *J. Materiomics*. **6**, 1–16. https://doi.org/10.1016/j.jmat.2019.11.001 (2020).
16. Ji, D. et al. Freestanding crystalline oxide perovskites down to the monolayer limit. *Nature*. **570**, 87–90. https://doi.org/10.1038/s41586-019-1255-7 (2019).
17. Lu, D. et al. Synthesis of freestanding single-crystal perovskite films and heterostructures by etching of sacrificial water-soluble layers. *Nat. Mater.* **15**, 1255–1260. https://doi.org/10.1038/nmat4749 (2016).
18. Li, R. et al. Preparation and characterization of a flexible ferroelectric tunnel junction. *Appl. Phys. Lett.* **116**. https://doi.org/10.1063/5.0006638 (2020).
19. Joh, H., Jung, M., Hwang, J., Goh, Y. & Jung, T. Jeon. Flexible ferroelectric Hafnia-based synaptic transistor by Focused-Microwave Annealing. *ACS Appl. Mater. Interfaces*. **14**, 1326–1333. https://doi.org/10.1021/acsami.1c16873 (2022).
20. Liu, B. et al. Excellent HZO ferroelectric thin films on flexible PET substrate. *J. Alloys Compd.* **919**. https://doi.org/10.1016/j.jallcom.2022.165872 (2022).

21. Liu, H. et al. Flexible quasi-van Der Waals Ferroelectric Hafnium-based oxide for Integrated High-Performance Nonvolatile Memory. *Adv. Sci. (Weinh)*. **7**. https://doi.org/10.1002/advs.202001266 (2020).
22. Liu, X. et al. A BaTiO3-based flexible ferroelectric capacitor for non-volatile memories. *J. Materiomics*. **11** https://doi.org/10.1016/j.jmat.2024.04.001 (2025).
23. Wu, J. et al. Flexible lead-free $BaTiO_3$ ferroelectric elements with high performance. *IEEE Electron Device Lett.* **40**, 889–892. https://doi.org/10.1109/led.2019.2911956 (2019).
24. Gao, W. et al. Flexible $PbZr_{0.52}Ti_{0.48}O_3$ capacitors with giant piezoelectric response and dielectric tunability. *Adv. Electron. Mater.* **3**https://doi.org/10.1002/aelm.201600542 (2017).
25. Jiang, J. et al. Flexible ferroelectric element based on Van Der Waals heteroepitaxy. *Sci. Adv.* **3**https://doi.org/10.1126/sciadv.1700121 (2017).
26. Qi, H. et al. Ferroelectric properties of the flexible pb$(Zr_{0.52}Ti_{0.48})O_3$ thin film on mica. *J. Mater. Sci.: Mater. Electron.* **31**, 3042–3047. https://doi.org/10.1007/s10854-019-02848-y (2020).
27. Renuka, H. et al. Enhanced photovoltaic response in ferroelectric Ti-doped BFO heterojunction through interface engineering for building integrated applications. *Sol. Energy*. **225**, 863–874. https://doi.org/10.1016/j.solener.2021.08.002 (2021).
28. Yang, C., Han, Y., Qian, J., Cheng, Z. & Flexible temperature-stable, and fatigue-endurable $PbZr_{0.52}Ti_{0.48}O_3$ ferroelectric film for nonvolatile memory. *Adv. Electron. Mater.* **5**. https://doi.org/10.1002/aelm.201900443 (2019).
29. Sun, H. et al. $BiFeO_3$-Based flexible ferroelectric memristors for Neuromorphic Pattern Recognition. *ACS Appl. Electron. Mater.* **2**, 1081–1089. https://doi.org/10.1021/acsaelm.0c00094 (2020).
30. Bai, F. et al. Destruction of spin cycloid in (111) c-oriented $BiFeO_3$ thin films by epitiaxial constraint: enhanced polarization and release of latent magnetization. *Appl. Phys. Lett.* **86**. https://doi.org/10.1063/1.1851612 (2005).
31. Song, J. et al. Enhancement of Ferroelectric properties of Superlattice-based Epitaxial $BiFeO_3$ Thin films via Substitutional Doping Effect. *J. Phys. Chem. C.* **123**, 11564–11571. https://doi.org/10.1021/acs.jpcc.9b00156 (2019).
32. Zhu, H., Zhao, Y. & Wang, Y. Orientation dependent leakage current behaviors and ferroelectric polarizations of off-axis sputtered $BiFeO_3$ thin films. *J. Alloys Compd.* **803**, 942–949 https://doi.org/10.1016/j.jallcom.2019.06.343(2019).
33. Kyun Lee, S., Ho Choi, B. & Hesse, D. Epitaxial growth of multiferroic $BiFeO_3$ thin films with (101) and (111) orientations on (100) Si substrates. *Appl. Phys. Lett.* **102**, 361–728. https://doi.org/10.1063/1.4811484 (2013).
34. Maeng, W. J. & Son, J. Y. Highly (111)-oriented multiferroic $BiFeO_3$ thin film on a glass substrate. *J. Cryst. Growth.* **367**, 24–26. https://doi.org/10.1016/j.jcrysgro.2013.01.012 (2013).
35. Chen, C. et al. Polarization fatigue of $BiFeO_3$ films with ferromagnetic metallic electrodes. *AIP Adv.* **7**https://doi.org/10.1063/1.4977761 (2017).
36. Simões, A. Z., Pianno, R. F., Aguiar, E. C., Longo, E. & Varela, J. A. Effect of niobium dopant on fatigue characteristics of $BiFeO_3$ thin films grown on pt electrodes. *J. Alloys Compd.* **479**, 274–279. https://doi.org/10.1016/j.jallcom.2009.01.074 (2009).
37. Yun, Q. et al. Improved ferroelectric and fatigue properties in Ho doped $BiFeO_3$ thin films. *Mater. Lett.* **129**, 166–169. https://doi.org/10.1016/j.matlet.2014.05.046 (2014).
38. Neaton, J. B., Ederer, C., Waghmare, U. V., Spaldin, N. A. & Rabe, K. M. First principles Study of spontaneous polarization in Multiferroic $BiFeO_3$. *Phys. Rev. B.* **71**https://doi.org/10.1103/PhysRevB.71.014113 (2005).
39. Liu, J. et al. Yang. Mechanically tunable magnetic properties of flexible $SrRuO_3$ Epitaxial Thin films on Mica Substrates. *Adv. Electron. Mater.* **4** https://doi.org/10.1002/aelm.201700522 (2018).
40. Liu, X., Pan, D., Hong, Y. & Guo, W. Bending Poisson Effect in two-dimensional crystals. *Phys. Rev. Lett.* **112**https://doi.org/10.1103/PhysRevLett.112.205502 (2014).
41. Yang, Y. et al. Flexible, semitransparent, and Inorganic Resistive Memory based on $BaTi_{0.95}Co_{0.05}O_3$ Film. *Adv. Mater.* **29**, 1700425. https://doi.org/10.1002/adma.201700425 (2017).
42. Botea, M. et al. Lead-free $BiFeO_3$ Thin Film: ferroelectric and pyroelectric properties. *Electron. Mater.* **3**, 173–184. https://doi.org/10.3390/electronicmat3020015 (2022).
43. Hou, P., Wang, J. & Zhong, X. Investigation of multilevel data storage in silicon-based polycrystalline ferroelectric tunnel junction. *Sci. Rep.* **7**, 4525. https://doi.org/10.1038/s41598-017-04825-z (2017).
44. Wang, Y. & Nan, C. W. Enhanced ferroelectricity in Ti-doped multiferroic $BiFeO_3$ thin films. *Appl. Phys. Lett.* **89** https://doi.org/10.1063/1.2222242 (2006).
45. Yang, N. et al. Nonvolatile negative optoelectronic memory based on Ferroelectric Thin films. *ACS Appl. Electron. Mater.* **2**, 1035–1040. https://doi.org/10.1021/acsaelm.0c00066 (2020).
46. Zhao, Z. et al. Flexible artificial synapse based on single-crystalline $BiFeO_3$ thin film. *Nano Res.* **15**, 2682–2688. https://doi.org/10.1007/s12274-021-3782-4 (2021).
47. Yang, Y. et al. The role of ferroelectric polarization in resistive memory properties of metal/Insulator/semiconductor tunnel junctions: a comparative study. *ACS Appl. Mater. Interfaces*. **12**, 32935–32942. https://doi.org/10.1021/acsami.0c08708 (2020).
48. Hu, Z. et al. Ferroelectric memristor based on Pt/BiFeO3/Nb-doped $SrTiO_3$ heterostructure. *Appl. Phys. Lett.* **102**, 102901. https://doi.org/10.1063/1.4795145 (2013).
49. Li, C. et al. Ultrathin $BaTiO_3$-based ferroelectric tunnel junctions through interface engineering. *Nano Lett.* **15**https://doi.org/10.1021/acs.nanolett.5b00138 (2015).
50. Ma, C. et al. Sub-nanosecond memristor based on ferroelectric tunnel junction. *Nat. Commun.* **11**. https://doi.org/10.1038/s41467-020-15249-1 (2020).
51. Wang, Z. et al. High-speed Nanoscale ferroelectric tunnel Junction for Multilevel memory and neural Network Computing. *ACS Appl. Mater. Interfaces*. **14**, 24602–24609. https://doi.org/10.1021/acsami.2c04441 (2022).
52. Morozovska, A. N., Eliseev, E. A., Kalinin, S. V., Vysochanskii, Y. M. & Maksymovych, P. Stress-induced phase transitions in nanoscale $CuInP_2S_6$. *Phys. Rev. B.* **104**. https://doi.org/10.1103/PhysRevB.104.054102 (2021).
53. Chen, Q. et al. Significantly enhanced energy storage density and efficiency in flexible $Bi_{3.15}Nd_{0.85}Ti3O_{12}$ thin film via periodic dielectric layers. *J. Appl. Phys.* **131**. https://doi.org/10.1063/5.0080321 (2022).
54. Zuo, Z. et al. Preparation and ferroelectric properties of freestanding pb(zr,Ti)O_3 thin membranes. *J. Phys. D Appl. Phys.* **45**, 185302. https://doi.org/10.1088/0022-3727/45/18/185302 (2012).

Acknowledgements

Project support by National Natural Science Foundation of China (Nos. 62174041, 62361022, 52262022), Guangxi Natural Science Foundation (NO.2023GXNSFBA026216), Guangxi Science and Technology Plan Project (AD24010060), Guangxi Key Laboratory of Information Materials & Guangxi Collaborative Innovation Center of Structure and Property for New Energy Materials (No. 231015-Z).

Author contributions
Yiming Peng was responsible for writing the original manuscript, Xingpeng Liu for designing the experiments, Tangyou Sun and Fabi Zhang for compiling the experimental data, and Ying Peng and Haiou Li for proofreading the article. Lei Wen helped in the rework process.All authors contributed to the study. All authors read and approved the final manuscript.

Declarations

Competing interests
The authors declare no competing interests.

Additional information
Supplementary Information The online version contains supplementary material available at https://doi.org/10.1038/s41598-024-77119-w.

Correspondence and requests for materials should be addressed to Y.P., L.W. or H.L.

Reprints and permissions information is available at www.nature.com/reprints.

Publisher's note Springer Nature remains neutral with regard to jurisdictional claims in published maps and institutional affiliations.

Open Access This article is licensed under a Creative Commons Attribution-NonCommercial-NoDerivatives 4.0 International License, which permits any non-commercial use, sharing, distribution and reproduction in any medium or format, as long as you give appropriate credit to the original author(s) and the source, provide a link to the Creative Commons licence, and indicate if you modified the licensed material. You do not have permission under this licence to share adapted material derived from this article or parts of it. The images or other third party material in this article are included in the article's Creative Commons licence, unless indicated otherwise in a credit line to the material. If material is not included in the article's Creative Commons licence and your intended use is not permitted by statutory regulation or exceeds the permitted use, you will need to obtain permission directly from the copyright holder. To view a copy of this licence, visit http://creativecommons.org/licenses/by-nc-nd/4.0/.

© The Author(s) 2024